

# Confinement-induced proliferation of vortices around marine invertebrate larvae

Bikram D. Shrestha<sup>1†</sup>, Santhan Chandragiri<sup>1†</sup>,  
Christian D. Gibson<sup>1</sup>, Nina R. Couture<sup>1</sup>, Melissa Ruszczyk<sup>1</sup>,  
Vivek N. Prakash<sup>1,2,3\*</sup>

<sup>1</sup>Department of Physics, College of Arts and Sciences, University of  
Miami, Coral Gables, FL, USA.

<sup>2</sup>Department of Biology, College of Arts and Sciences, University of  
Miami, Coral Gables, FL, USA.

<sup>3</sup>Department of Marine Biology and Ecology, Rosenstiel School of Marine,  
Atmospheric, and Earth Science, University of Miami, Miami, FL, USA.

\*Corresponding author(s). E-mail(s): [vprakash@miami.edu](mailto:vprakash@miami.edu);

†These authors contributed equally to this work.

## Abstract

The ocean is teeming with a myriad of submillimeter-sized invertebrate planktonic larvae [1], which thrive in a viscous fluid environment [2]. Many of them rely on ciliary beating to generate fluid flows for locomotion and feeding [2, 3]. Their forms, local morphologies, and ciliation patterns exhibit remarkable diversity [4], producing intricate and dynamic three-dimensional (3D) flows that are notoriously difficult to characterize in laboratory settings. Traditional microscopic imaging techniques typically involve gently squeeze-confining the soft larvae between a glass slide and cover slip, to study their flows in quasi-two-dimensions (2D) [5]. However, a comprehensive hydrodynamic framework for the low-to-intermediate Reynolds number ( $< \sim 1$ ) flows at the larval scale in quasi-2D confinement—particularly in light of their complex forms—has remained elusive. Here, we demonstrate that vortices around larvae proliferate with increasing confinement, and elucidate the underlying physical mechanism. We experimentally quantify confinement-induced flows in larvae of sea stars and sea urchins. The flows exhibited strikingly universal patterns: under weak confinement, all larvae generated two vortices, whereas under strong confinement, multiple vortices appeared. The experimental observations were well captured by a low Reynolds number theoretical model based on superposition of confined Stokeslets [6, 7]. Building on experiments and theory, we developed a comprehensive framework

for confinement-induced larval flows, which suggests that the vorticity dynamics are primarily determined by local morphological features, rather than the larval forms. Our work provides fundamental insights into the form-functional relationships between larval morphology and flow generation. Our findings are broadly applicable to understanding fluid flows generated by a wide range of ciliated organisms with complex forms and morphologies, from micro- to milli-length-scales.

**Keywords:** Biomechanics, Fluid dynamics, Marine invertebrate larvae, Confinement, Ciliary flows

Diverse and exotic life forms inhabit the vast oceans and hold many secrets to life that are waiting to be unraveled [1]. The biomechanics of marine animals and their interactions with the fluid environment are fundamental drivers of ecological and evolutionary processes in the ocean. Marine species generate fluid flows for a variety of purposes, including locomotion, feeding, predator evasion, reproduction, and development [2, 8–11]. Many benthic marine invertebrates, such as echinoderms (e.g. sea stars and sea urchins) undergo an indirect mode of development that involves a pelagic larval stage with a form completely different from their adult form. During this larval stage, these organisms swim and feed in the water column for weeks or even months, before metamorphosing into their adult shape. The majority of these larvae are soft-bodied planktonic free-swimmers that utilize ciliary beating to create fluid flows that are used for both swimming and feeding [3, 5, 12]. In these larvae, large numbers of motile cilia are arranged in ‘ciliary bands’ that are intricately embedded in their body morphologies, and enable them to generate unexpectedly rich fluid-flow patterns. So far, sea star larvae have been shown to generate a fascinating array of multiple counter-rotating vortices around them [5, 13]. Further, the diversity of ciliated larval forms is staggering, with remarkable variations in body morphology and ciliation patterns [4]. Therefore, an open question is whether the differences in forms and local morphologies between ciliated larvae give rise to distinct flow patterns? We will investigate this question for the first time by examining morphologically distinct larvae from two closely related echinoderms: the sea star (*Patiria miniata*) and sea urchin (*Lytechinus variegatus*). Specifically, we will investigate two developmental stages (Early-stage and Late-stage) of sea star larvae, and one stage of sea urchin larvae. The sea star larvae have an oval/ellipsoid form, with bilateral and anterior-posterior symmetry; the Early-stage bipinnaria larvae have a simpler morphology compared to the more complex-shaped Late-stage brachiolaria larvae, which feature short arms. In stark contrast, the echinopluteus sea urchin larvae have a cone-shaped form, with rigid, extended skeletal arms and exhibit bilateral symmetry but lack anterior-posterior symmetry. In this study, we aim to experimentally quantify and model the flow patterns generated by these three distinct larval types, seeking to uncover the fundamental relationships between the different forms of marine invertebrate larvae and their hydrodynamic signatures.

The tiny submillimeter-size larvae reside in a viscous fluid environment in the ocean, where viscous forces dominate over inertial forces. This balance is quantified

by the Reynolds number ( $Re$ ), which represents the ratio of inertial to viscous forces, and is defined as  $Re = UL/\nu$ , where  $U$ ,  $L$ , and  $\nu$  are the characteristic velocity, length scale, and kinematic viscosity of water, respectively. For sea star and sea urchin larvae swimming in seawater,  $Re \sim 0.1\text{--}0.9$  (Table 1, Supplementary Information), placing them within a low-to-intermediate Reynolds number regime, where although viscous effects are prominent, inertial effects are also starting to play a role. Low-to-intermediate Reynolds number flows represent a relatively under-explored regime in fluid dynamics, as the majority of the existing literature on biological fluid mechanics focuses on either low Reynolds number flows [2, 3, 14] or intermediate to high Reynolds number flows [8, 9]. In this study, we present new experimental results at  $Re \sim 0.1\text{--}0.9$ , and demonstrate that theoretical models based on low Reynolds number assumptions are able to provide a qualitatively accurate description of the observed phenomena.

The majority of aquatic microorganisms, ranging from micro- to milli-scale, swim at low-to-intermediate Reynolds numbers freely in three dimensions (3D) within open water bodies such as lakes and oceans. However, these microorganisms frequently encounter rigid boundaries or surfaces due to interactions with other living organisms or non-living structures, such as the air-water interface or other solid matter, including substrates at the bottom. Microorganism-boundary interactions have significant biological implications in various natural contexts. For example, sessile, suspension-feeding ciliated organisms like *Vorticella* [15, 16], *Stentor* [17], and *Coral* [18, 19] need to optimize nutrient availability in their immediate surroundings. Similarly, many organisms rely on internal ciliary-driven flows within ducts to regulate vital physiological processes [20]. The marine invertebrate larvae examined in this study likely come across rigid boundaries primarily during terminal encounters or in laboratory settings. Nevertheless, they serve as an excellent model system for investigating the hydrodynamic effects of microorganism-boundary interactions. Confinement-induced fluid dynamical phenomena are often found to be highly non-intuitive and non-trivial, garnering considerable interest in the field of biological fluid dynamics, particularly at low Reynolds numbers [5–7, 15–17, 21–30]. In the present work, we investigate confinement effects in low-to-intermediate Reynolds number flows for the first time.

The complex 3D flow-fields generated by ciliated marine invertebrate larvae pose significant challenges for quantification in laboratory-based experimental studies, even though there have been recent advancements [31]. The straightforward traditional microscopic imaging methods, which confine larvae between a glass slide and a cover slip, impose a quasi-two-dimensional (2D) confinement. So far, this conventional quasi-2D approach has been instrumental in revealing phenomena such as the multiple vortex arrays generated by sea star bipinnaria larvae [5]. However, alternative confinement techniques, such as tethering larvae [24], fail to produce the same multiple vortex patterns [5, 13, 25]. This discrepancy raises fundamental questions about the impact of quasi-2D confinement on the flow fields of 3D micro-swimmers. Here, we resolve this conundrum and address several longstanding questions that have puzzled biological fluid mechanics for decades: How does quasi-2D confinement alter the fluid flow fields of a 3D micro-swimmer? Do variations in geometric form and local morphology of ciliated larval micro-swimmers give rise to different flow patterns under quasi-2D

confinement? Is there a unified theoretical hydrodynamic framework that can capture these quasi-2D confinement effects at low-to-intermediate Reynolds numbers?

We address these open questions in physics and biology by investigating the effects of squeeze-confinement on the low-to-intermediate Reynolds number flows generated by three distinct forms of ciliated marine invertebrate larvae of echinoderms: (i) Early-stage sea star, (ii) Late-stage sea star, and (iii) Sea urchin (Fig. 1). We systematically vary the confinement parameter—the height between the glass slide and cover slip ( $H$ )—and quantify changes in the vorticity dynamics. We quantitatively compare our experimental results with a theoretical low Reynolds number-based model, and develop a universal hydrodynamic framework for confinement flows.

## Confinement-induced flows in marine larvae

Using live darkfield time-lapse microscopy experiments, we observed that the flow-fields generated by the three distinct larvae varied depending on the degree of squeeze-confinement (Methods, Fig. 1). The larvae were confined by gently trapping or squeezing them in between a glass slide and a cover slip that were separated by a precisely known height 'H', i.e. the squeeze-confinement parameter. This confinement parameter was varied over a broad range for the three larvae – from 'weak confinement' (low squeeze/large H) to 'strong confinement' (high squeeze/small H) and their resultant flow-fields were quantified using standard techniques from experimental fluid dynamics (Fig. 1, Methods). The flow visualizations in Fig. 1 (a-f) were carried out by post-processing of the time-lapse images using Flowtrace in ImageJ [32] (left panels), and Particle Image Velocimetry (PIV) in MATLAB [33] (right panels) (Methods). We observed that weak confinement (low squeeze/large H) resulted in two vortices in all the three types of larvae (Fig. 1 a,c,e) (Video 1). When the confinement was increased by bringing the glass slide and cover slip closer, first reaching 'moderate' confinement conditions (medium squeeze/medium H) (Extended Data Fig. 1) and then going to 'strong' confinement conditions (high squeeze/small H), all the larvae generated more than two vortices (Fig. 1 b,d,f) (Video 2). In our quasi-2D experiments, the thin imaging z-plane was focused close to the mid-plane ( $\sim H/2$ ) located in between the bottom (glass slide) and top (cover slip) boundaries. We found that there was minimal flow field variation in the z-planes above and below the mid-plane (Extended Data Fig. 2). Hence our experiments captured the dominant and representative quasi-2D flow fields generated by the larvae.

To account for the size variation among the three types of larvae, we divide the confinement height 'H' length scale with the larval depth dimension 'c', to arrive at a normalized squeeze-confinement parameter  $H/c$  (Supplementary Information). This non-dimensional confinement parameter  $H/c$  provides a standardized quantification of the degree of squeeze-confinement, and hence enables comparison of flows between the three larval types. We found that weak confinement (squeeze parameter,  $H/c \sim 1$ ) always resulted in a fixed number of vortices (two) being generated by the larvae, irrespective of their form and local morphology (Fig. 1 a,c,e). However, when the strength of confinement was increased (squeeze parameter,  $H/c < 1$ ), the total number of vortices generated varied depending on the degree of confinement and the larval form and local morphology (Fig. 1 b,d,f). Under strong confinement ( $H/c \ll 1$ ) conditions,



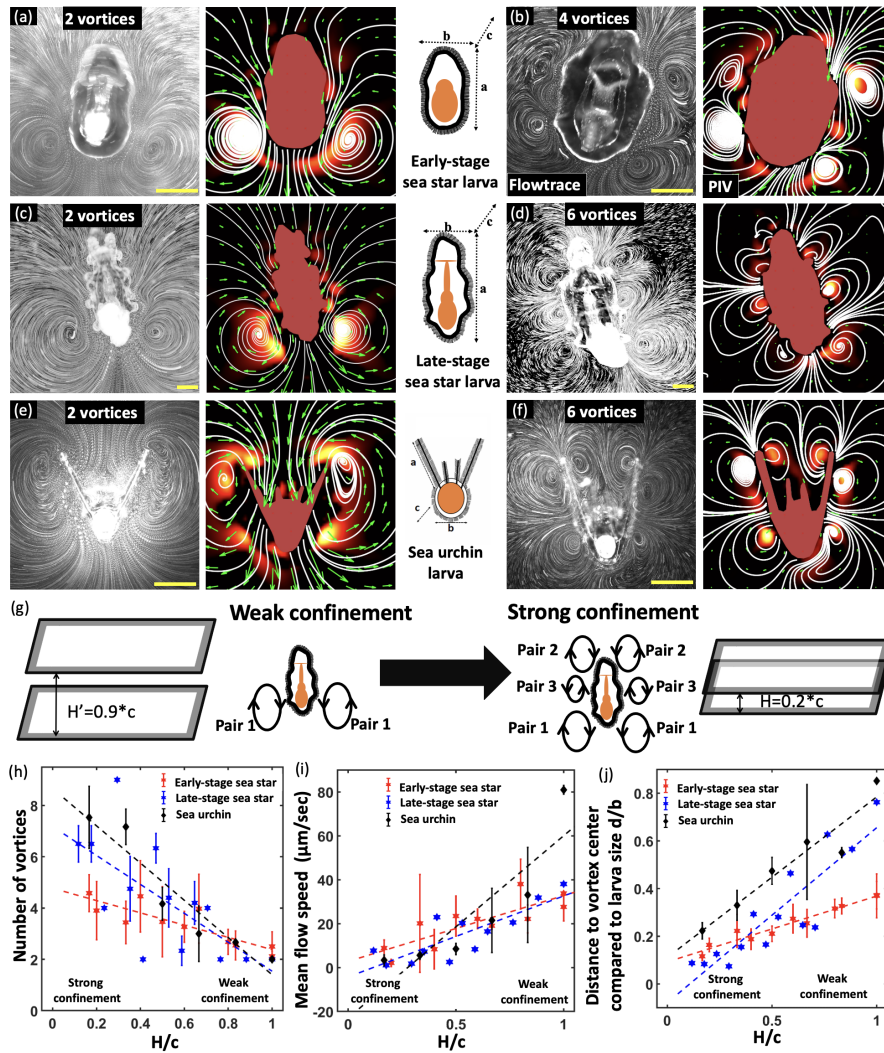


**Fig. 1: Fluid flow vortices generated by ciliated marine larvae in quasi-2D squeeze confinement experiments.** (a,b): Early-stage sea star larvae generate two vortices under weak confinement (a), and four vortices under strong confinement (b). (c,d): Late-stage sea star larvae generate two vortices under weak confinement (c), and six vortices under strong confinement (d). (e,f): Sea urchin larvae generate two vortices under weak confinement (e), and six vortices under strong confinement (f). In a-f, left panel shows flowtrace visualizations [32], and the right panels display corresponding flow fields obtained using Particle Image Velocimetry (PIV) [33]. PIV panels show streamlines (white) superimposed with velocity vector field (green arrows), larval masks (red color), and vortex locator heat map. (g) Schematic representation of changes in confinement parameter, 'H', the height between the glass slide and cover slip. Left panels show weak confinement (low squeeze) and the right panels show strong confinement (high squeeze), along with pairs of vortices generated. (h-j): Flow field quantification in different confinement regimes (weak, moderate and strong), displaying total number of vortices, mean flow speed, and distance from vortex center to larval body, as a function of squeeze confinement parameter ( $H/c$ ), where 'c' is the larval size in depth (z) dimension. The data points represent mean values and errorbars represent standard deviations. The length scale bars in a-f (yellow color) correspond to 0.2 mm.

the simple-shaped Early-stage sea star larva developed four total vortices, i.e. two symmetric pairs (Fig. 1 b). Although the complex-shaped Late-stage sea star and Sea urchin larvae developed a total of six vortices under strong confinement ( $H/c \ll 1$ ) (Fig. 1 d,f), the vortex locations were not similar since these two larvae have completely different forms and complex morphologies. Meanwhile, in the moderate confinement regime ( $H/c \sim 0.5$ ), the three different types of larvae generated more than two vortices (Extended Data Fig. 1), but less than the maximum number they generated under strong confinement (Fig. 1 b,d,f). Taken together, these results suggest that both the confinement parameter and larval morphology play an important role in determining vortex dynamics under confinement.

Further quantification of the confinement-induced fluid flows reveals several interesting common trends. The total number of vortices generated over a range of confinement parameters  $H/c$  (0.1–1) was determined using a large number of samples from our experiments (Fig. 1 h) (Extended Data Fig. 3 a,b) (Table 1, Supplementary Information). Irrespective of the larval form and morphology, we observed that weak confinement ( $H/c \sim 1$ ) always resulted in 2 vortices. However, when the degree of squeeze-confinement was increased ( $H/c < 1$ ), the number of vortices increased with an almost linear trend (inferred via linear fits) with slightly different slopes for all the three larvae (Fig. 1 h). Under the strongest squeeze-confinement conditions ( $H/c \sim 0.2$ ) (Fig. 1 h), both the morphologically complex Sea urchin larvae with extended arms, and the morphologically complex Late-stage sea star larvae, developed a maximum of nine vortices (Fig. S1, Supplementary Information). However, the morphologically less complex Early-stage sea star larvae only generated a maximum of six vortices (Fig. S1, Supplementary Information). Overall, our results reveal that all the three types of larvae generate two vortices under weak confinement, and the number of vortices increase with confinement following an almost linear trend despite significant variations in their form and local body morphology (Fig. 1 h). From a physical perspective, these results suggest that more number of vortices are generated due to increased frictional effects when the top (cover slip) and bottom boundaries (glass slide) come closer to each other. Hence, we believe that this general trend of number of vortices increasing with increased confinement is universal and can be applicable to a wide majority of marine ciliated larvae at comparable sizes. Also, the intricate details of the larva’s local body morphology seems to determine the slope of the linear trend, with the most complex larval morphologies generating the largest number of vortices under strong confinement.

In addition to the total number of vortices generated, the larval flow-fields under different confinement conditions also showed systematic variations in other flow metrics such as the mean flow speeds generated (Fig. 1 i), and center locations of vortices (Fig. 1 j) (Methods). We observed that the mean flow speeds were maximum under weak confinement ( $H/c \sim 1$ ), and the speeds decreased almost linearly with increasing confinement ( $H/c < 1$ ) (Fig. 1 i, Extended Data Fig. 3 c). This trend can be attributed to an increase of frictional effects from the walls due to increased confinement ( $H/c < 1$ ), leading to suppression of the strength of fluid flows (speeds) generated by the larvae. We also observed that Sea urchin larvae generate fluid flows of higher mean speeds compared to the sea star larvae under weak confinement (Fig. 1 i), and

this is also reflected in the different slopes of linear fits for the three larvae. Next, our quantification of the distances from vortex centers to the larval body surface, also showed a maximum value under weak confinement ( $H/c \sim 1$ ), and a similar decreasing linear trend with increased confinement ( $H/c < 1$ ) (Fig. 1 j, Extended Data Fig. 3 d). This result implies that the vortices come closer to the larval body surface with increase in confinement and vice-versa. Finally, we also quantified the mean vorticity and circulation generated by the three larvae, and once again found a similar trend of linear decrease in values with increased confinement (Extended Data Fig. 2 e,f). Hence, all our experimental flow quantification results support our physical interpretation of increasing frictional effects from the walls due to increased confinement. Overall, these experimental results suggest the existence of an underlying hydrodynamic mechanism that determines the vortical flow patterns under different confinement conditions.

## Experimental and Theoretical Flow Quantification

In order to investigate the hydrodynamics of the confinement-induced flow fields in the larvae, we quantified the vorticity in the experimental data and developed a theoretical model that closely captures the experimental flow-fields. The hydrodynamic regime is quantified by the Reynolds number ( $Re$ ), which is a ratio of inertial to viscous forces, given by  $Re = UL/\nu$ , where  $U$  and  $L$  are the characteristic velocity and length scales, and  $\nu$  is the kinematic viscosity of the fluid. The  $Re$  for the three types of marine larvae studied here are in the range  $Re \sim 0.1 - 0.9$  (Methods, Supplementary Information, Table 1), which corresponds to a low-to-intermediate  $Re$  range where the flows are more dominated by viscous forces compared to inertial forces. Hence, we adopted a recently developed low  $Re$  hydrodynamics model [7] to quantitatively compare the experimental results. The model based on the quasi-2D Stokes equation for low  $Re$  flows consists of superposition of pairs of Stokeslets between two parallel flat plates, and explicitly takes into account the swimmer (larva) force  $F$ , and the chamber height  $H$  (squeeze-confinement parameter) [6, 7]. The final velocity field expressed in polar coordinates  $(r, \phi)$  is given by:

$$\begin{bmatrix} v_x \\ v_y \end{bmatrix} (r, \phi) = \frac{F}{2\pi^2\eta} \int_{-\pi/2+\phi}^{\pi/2+\phi} d\theta \int_0^\infty dk \begin{bmatrix} \sin^2 \theta \\ \sin \theta \cos \theta \end{bmatrix} \frac{k \cos [kr \cos (\theta - \phi)]}{(k^2 + \frac{\pi^2}{H^2})}$$

where,  $v_x, v_y$  are the velocity components in  $x, y$  directions, and  $\eta$  is the dynamic viscosity of the fluid. We input values for the force ( $F$ ) and chamber height ( $H$ ) corresponding to experiments into the theoretical model to compare the experimental flow-field results (Methods, Supplementary Information).

The comparison of the flow-field results obtained from PIV-analysis of our experimental data [33, 34] and our theoretical model are shown in Fig. 2. In weak confinement experiments ( $H/c < 1$ ), all the larvae – Early-stage and Late-stage sea star, Sea urchin – in spite of their distinct forms and local morphological variations, generated one dominant (large) pair of counter-rotating vortices (Pair 1) (Fig. 2 a, c, e, left panels).

In the oval-shaped Early-stage sea star larva and more complex-shaped Late-stage sea star larva under weak confinement, the pair of vortices are roughly circular-shaped, and their centers are located towards the back-end of the body (Fig. 2 a, c, left panels).

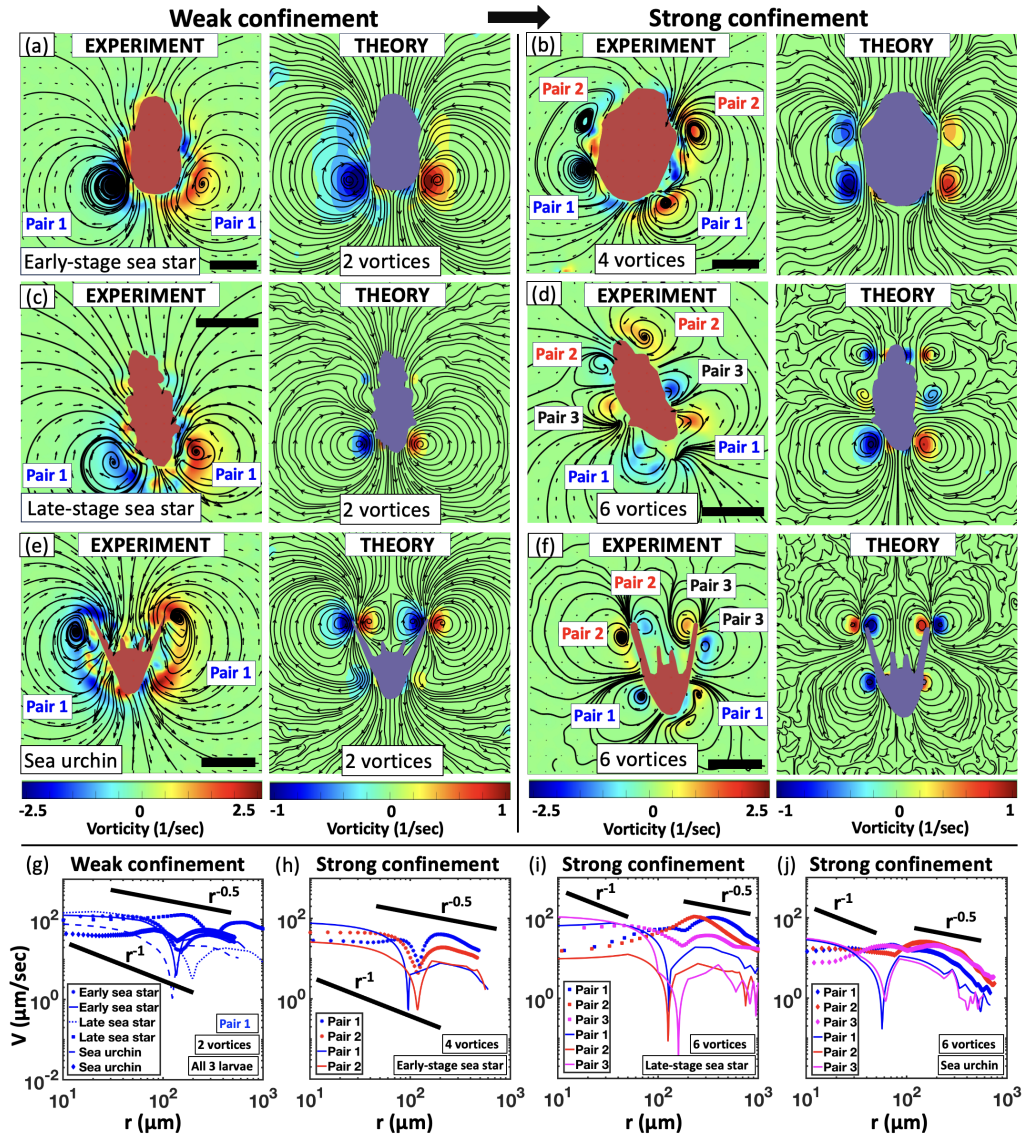


**Fig. 2: Experimental and theoretical quantification of confinement-induced fluid flows in marine larvae.** (a-f) First, second and third rows show comparison of flow-fields obtained from Experiments (PIV-derived vorticity) and Theory (superposition of Stokeslets) under weak and strong confinement for Early-stage sea star, Late-stage sea star, and Sea urchin larvae (masked in red/blue colors). (a,c,e) Experiments and theory show only two vortices (Pair 1) being generated under weak confinement in all three types larvae. (b,d,f) Under strong confinement, Early-stage sea star larvae create four vortices, and both Late-stage sea star and Sea urchin larvae create six vortices. The additional pairs of vortices (Pair 2 and 3) are also indicated. (g-j) Velocity quantification comparing experiments and theory: plots represent decay of velocity magnitude along a line perpendicular to the larval body surface and passing through the vortex center in Experiments (symbols) and theory (lines). Velocity decay curves corresponding to Pair 1, Pair 2, and Pair 3 vortices are represented by blue, red, and magenta curves. The solid lines represent the velocity decay scaling  $v \sim r^{-1}$  and  $v \sim r^{-0.5}$ . The length scale bars in Experimental panels (a-f) correspond to 0.2 mm.



The theoretical model utilized two pairs of Stokeslets for Early-stage sea star and three pairs of Stokeslets for the Late-stage sea star larvae under the same experimental confinement conditions ( $H$ ), and physical location around the body surface (Methods, Supplementary Information), and showed excellent agreement with the experiments for both types of sea star larvae (Fig. 2 a, c, right panels) (Extended Data Fig. 4 a,d). It must be noted that in the theoretical model, each Stokeslet generates 1 pair of vortices. However, the resultant velocity field due to the superposition of multiple Stokeslets gave rise to a flow field consisting of two vortices under weak confinement, closely matching the experiments (Extended Data Fig. 4, Methods, Supplementary Information).

However, in Sea urchin larvae, weak confinement resulted in vortices that are highly elongated in an ellipsoidal shape and distributed over the sides of the arms. In addition, the vortex centers are located near the tip of the extended arms (Fig. 2 e left panel). The theoretical model here utilized two pairs of Stokeslets under the same experimental confinement conditions ( $H$ ) and physical location at the tip of the extended arms (Methods, Supplementary Information), and showed a flow-field comparable in magnitude with the experiments, but not in the number of vortices generated (Fig. 2f right panel). Compared to the sea stars, the Sea urchin larval morphology is much more complex, with with extended rigid arms. In this developmental stage, the Sea urchin larva also had two small rudimentary arms near its oral surface, and these could also potentially influence the observed flow- fields. For simplicity, the theoretical model does not account for the presence of these small arms. Hence, the theoretical flow-fields are slightly different from that of experiments. Overall, each of the experimental larval vortices under weak confinement can be modeled theoretically with the superposition of multiple Stokeslets, and the experimental two-vortex larval flow-field could be captured accurately.

Under strong confinement conditions ( $H/c \ll 1$ ), the local morphological variations between the three larvae play an important role in the number of vortices generated (Fig. 2 b, d, f, left panels). While the Early-stage sea star generates two pairs of vortices (Pairs 1,2) (Fig. 2 b), both the Late-stage sea star and Sea urchin larvae generate three pairs of vortices (Pairs 1,2,3) (Fig. 2 d, f). Hence, strong confinement promotes the development of additional pairs of vortices in all the larvae (Fig. 2 b, d, f). The Early-stage sea star larva has a oval/ellipsoid-shaped form, and although it does not yet have arms protruding outside the body, there is a sharp convex curvature change in the region where arms will be formed in the future. The theoretical model with two pairs of Stokeslets placed at exactly the region corresponding to the convex curvature change shows an excellent agreement with the experiments (Fig. 2 b, right panel).

In addition to the oval-shaped body, the Late-stage sea star larvae also have protruding arms which act as localized sources of vorticity generation. Hence, under strong confinement, these larvae generate three pairs of vortices (Pairs 1,2,3) (Fig. 2 d, left panel). The theoretical model considering three pairs of Stokeslets placed exactly adjacent to the arms corresponding to the physical locations, once again shows excellent agreement with the experiments (Fig. 2d, right panel).

In the Sea urchin larvae, in addition to the tips of the extended arms, a hood region just below the arms also act as localized sources of vorticity generation. These morphological complexities enabled these larvae to generate three pairs of vortices (Pairs 1,2,3) under strong confinement (Fig. 2f left panel). To develop these three pairs of vortices in theory, a 2 pair Stokeslet model is used. In this context, one pair of Stokeslets are introduced at the back of the sea urchin larvae that accounted for the hood. Next, at the tip of each arm, one Stokeslet was introduced. Overall, this two pair Stokeslet model is able to capture the Sea urchin larval experimental flow-fields very well ((Fig. 2f left panel)).

Overall, the theoretical model using superposition of Stokeslets qualitatively captured the experimental results very well in all the three morphologically complex larvae in different confinement conditions, ranging from weak to high squeeze confinement. Further, the theoretical model was compared quantitatively with the experiments by calculating the magnitude of spatial velocity decay over the vortices (Fig. 2 g-j). Under weak confinement conditions ( $H/c < 1$ ), since all the three larvae generate only one pair of vortices (Pair 1), we compared their velocity magnitude decay through the two vortex centers (averaged over Pair 1) from both the experiments and theoretical model in Fig. 2g. For the three types of larvae, the velocity at the larval body surface starts in the range  $50\text{-}150 \mu\text{m s}^{-1}$  and decays to a minimum (sharp dip representing the vortex center), and eventually decays to about half of its magnitude ( $30\text{-}70 \mu\text{m s}^{-1}$ ) over a length scale of about  $1 \text{ mm}$  (Fig. 2g). For the Early-stage sea star, the theoretical model matches the experiments almost exactly, and for the Late-stage sea star and Sea urchin, the model is unable to match the experiments quantitatively, but still follows the overall trends. The velocity decays for all the types of larvae follow slopes in the range between  $v \sim r^{-1}$  and  $v \sim r^{-0.5}$ . The initial velocity decay is closer to  $v \sim r^{-1}$ , and after crossing the velocity dip at the vortex center, the decay becomes less steep with a slope closer to  $v \sim r^{-0.5}$  (Fig. 2g).

For strong confinement ( $H/c \ll 1$ ), the spatial velocity magnitude decays between the experiments and the theoretical model for the three types of larvae were compared for each vortex pair (Pair 1,2,3) separately (Fig. 2 h-j). The theoretical model has the best match for the Early-stage sea star, followed by the Sea urchin, and then the Late-stage sea star larvae. The experimental velocity decays from a range of  $8\text{-}35 \mu\text{m s}^{-1}$  at the surface to about half the value ( $3\text{-}15 \mu\text{m s}^{-1}$ ) for the Early-stage sea star and Sea urchin larvae (Fig. 2 h,j), but this trend does not hold for all vortex pairs in the Late-stage sea star larvae (Fig. 2 i). In all the three types of larvae, the theoretical model shows a steeper initial velocity decay of  $v \sim r^{-1}$  compared to the experimental data, but the decay slope of  $v \sim r^{-0.5}$  towards the end matches the experimental data (Fig. 2 h-j). In all the larvae, the model predicts a sharp dip in velocity at the vortex center, but only the Early-stage sea star experiments show this sharp dip (Fig. 2 h).

Our theoretical model captures the experimental velocity decay trends reasonably well, but not the magnitudes. For the three types of larvae, in both the weak and strong confinement conditions, although the theoretical model velocity decay slopes range between  $v \sim r^{-1}$  and  $v \sim r^{-0.5}$ , the experimental data more closely follow the  $v \sim r^{-0.5}$  decay (Fig. 2 g-j). In comparison, the velocity decays in the low Reynolds numbers flows in *Chlamydomonas reinhardtii* have been found to decay as  $v \sim r^{-2}$  [26],

which is also the expected velocity decay for a point source confined between two parallel no-slip walls [6, 26]. The less steep velocity decays observed in the present work, in the range between  $v \sim r^{-1}$  and  $v \sim r^{-0.5}$ , can most likely be attributed to inertial effects. Future theoretical work in this regime of low-to-intermediate Reynolds numbers ( $Re \sim 0.1-0.9$ ) is necessary to deepen our understanding of the physical mechanisms underlying the velocity decays.

## Framework for confinement-induced vorticity proliferation

The theoretical model described above using superposition of Stokeslets matched the experimental confinement-induced flows (Fig. 2) and revealed two key features of confinement-induced flows in the morphologically complex larvae of Sea stars and Sea urchin. First, under strong confinement, the theoretical model utilized a unit Stokeslet to represent a localized source of vorticity generation in the experiments, often corresponding to a morphological location on the larval body such as the convex curvature change in the Early-stage sea star larva, the protruding arms in Late-stage sea star larva, or the tip of extended arms in Sea urchin larvae (Fig. 2 b,d,f). Second, a quantitative comparison of the experimental confinement-induced velocity decays for all the types of larvae (Fig. 2 g-j) revealed that the velocity magnitudes under weak confinement are about five times higher than the velocity magnitudes under strong confinement. This result suggests that frictional effects from the bottom and top walls decrease the velocity magnitude as the walls come closer due to increase in confinement. Putting together these two key features, we present a general framework to explain the increase in number of vortices due to increase in confinement.

In the example of the Late-stage stage sea star larva, the body morphology consists of an extended oval/ellipsoidal shape with protruding arms. This Late-stage sea star larva generates two vortices under weak confinement (Fig. 1c, Fig. 2c), four vortices under moderate confinement (Extended Fig. 1), and six vortices under strong confinement (Fig. 1d, Fig. 2d). In Fig. 3 a-c, the vorticity field generated by the Late-stage sea star larva is reexamined for weak, moderate and strong confinements. The three source pairs (Pair 1,2,3) of local vorticity generation are visible in all the three confinement conditions. In weak confinement, the Pair 1 vortices dominate the flow-field with the largest vortex size (area) (Fig. 3d) (Extended Data Fig. 5 d) (Methods). However, the local sources of vorticity generation (Pairs 2 and 3) corresponding to the locations of the protruding arms are visible as small patches of vorticity (Fig. 3a,d). In moderate confinement, the frictional effects from the top and bottom walls are increased, which decreases the size of the dominant Pair 1 vortices (Fig. 3b,d), and in turn provides an opportunity for Pair 2 and 3 vortices to increase in size (Fig. 3d). However, only Pair 2 vortices are able to develop properly given that these are located far away from Pair 1. Hence, Pairs 1 and 2 dominate the flow field and suppress the formation of Pair 3 vortices (Fig. 3b). Under strong confinement, the wall frictional effects are further increased, and this further decreases the size of Pair 1 vortices (Fig. 3d), and enables the generation of Pair 3 vortices. Hence, the flow-field is dominated by all the three vortex Pairs (1,2,3), giving rise to a total of six vortices. The vortex size results for Early-stage sea star and Sea urchin larvae under weak, moderate, and strong confinement also show the same trend observed in Late-stage sea star larvae (Fig. 3e)



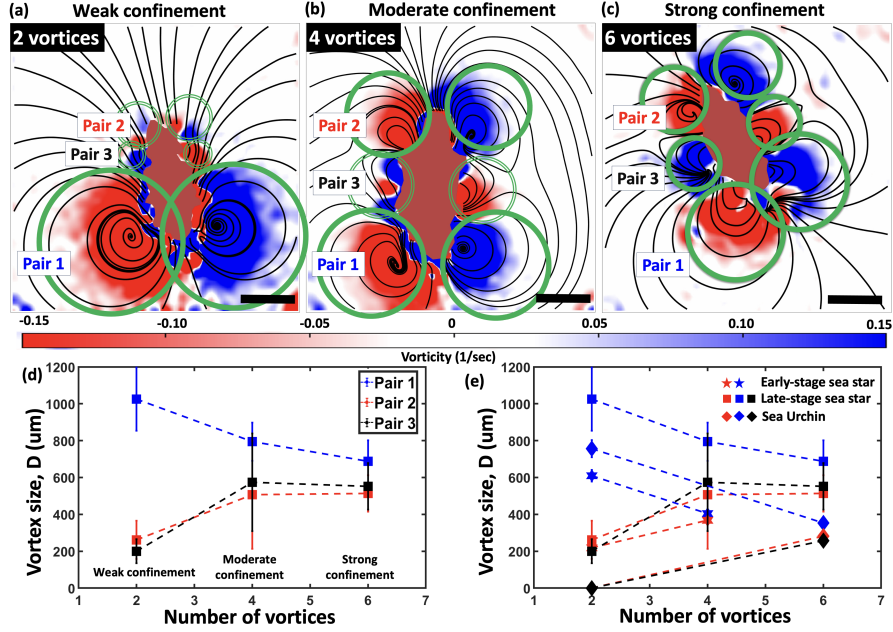


**Fig. 3: Local vorticity amplification with increasing confinement in experiments.** (a-c) In Late-stage sea star larvae, the three pairs of vorticity sources around the larval body from experiments are shown under the different squeeze-confinement conditions (weak, moderate and strong). (a) Only vortex pair 1 dominates, resulting in 2 vortices (solid green circles). (b) Vortex pairs 1 and 2 both dominate, resulting in 4 vortices (solid green circles). (c) All 3 vortex pairs are comparable, resulting in 6 vortices (solid green circles). (d) The vortex size, represented as a diameter ( $D$ ), as a function of total number of vortices generated around the Late-stage sea star larva (indirectly representing increase in confinement). The dominant Pair 1 vortex size decreases with increase in confinement, whereas Pair 2 and 3 vortices increase in size with increase in confinement. (e) Same plot as in (d), but with the addition of data points from Early-stage sea star larvae and Sea urchin larvae, which also show the same trends as in Late-stage sea star larvae. The length scale bars in panels (a-c) correspond to 0.5 mm.

(Extended Data Fig. 4)(Extended Data Fig. 5). Hence, the confinement-induced flow-fields show similar trends for the larvae of very different forms and local morphologies. This suggests that the phenomenon of increase in number of vortices due to increase in confinement, only depends on the number of sources of local vorticity generation that can either get suppressed or amplified depending on whether the confinement is weak or strong. Importantly, this phenomenon is independent of details of the overall global larval form but only dependent on the local sources of vorticity generation (local morphological features such as tips of arms, sharp convex regions, etc.).

In summary, we investigated the flow-fields induced by squeeze-confinement at low-to-intermediate Reynolds numbers ( $<\sim 1$ ) in the distinct larval forms of Early-stage

and Late-stage sea stars, and Sea urchins. In all three cases, the larvae generated two vortices under weak confinement, but under strong confinement they developed multiple vortices. A low Reynolds number-based theoretical model utilizing superposition of multiple Stokeslets showed good qualitative agreement with the experiments. Based on the experiments and theory, we constructed a framework to explain the universality of vortex dynamics under confinement, highlighting the importance of morphological features inducing local vorticity generation.

Hydrodynamics resulting from microorganism-surface interactions are intriguing and often give rise to non-intuitive physical phenomena. While the present work elucidates the fluid dynamics associated with larval squeeze-confinement, alternative confinement methods—such as tethering [21, 24, 25] or strong adhesive attachment [35]—could significantly alter the boundary conditions and lead to novel fluid dynamic effects. Also, the larval flows in the current work are in the regime of low-to-intermediate Reynolds numbers (0.1-0.9), so even though viscous effects are more important, inertial effects also need to be considered. Although our theoretical model based on low Reynolds numbers [6, 7] performs well qualitatively, it does not work quantitatively since the model does not account for inertial effects. Hence, there is a need for the development of a new class of theoretical microswimmer models in this low-to-intermediate Reynolds numbers regime.

Our study primarily relied on a quasi-2D flow approximation, which is well-suited for the larval scale. However, we anticipate that the complex morphologies of larvae will give rise to intricate localized flows in 3D, which could play a crucial role in swimming and feeding dynamics. Additionally, we have assumed that squeeze-confinement does not substantially affect local ciliary beating in our experiments, given that ciliary movement is likely regulated at the level of individual cells. These considerations highlight important avenues for future research and underscore the broader significance of these confinement-induced phenomena for the larval biology and biological fluid dynamics community.

Confinement-induced fluid dynamical effects on microorganisms can also have important biological consequences [5, 17]. Although it is unlikely that echinoderm larvae encounter squeeze-confinement conditions in the ocean, they are likely to interact with surfaces, and these hydrodynamic interactions can influence their swimming and feeding behaviors [5], which will be the focus of our future studies. Thus, while our fluid dynamics results are generally relevant to microswimmer-surface interactions, they are particularly applicable to quantitative laboratory-based studies involving microscopic confinement of a wide range of ciliated and motile marine microorganisms with varied forms and morphologies [17, 27], including collective phenomena that emerge when large numbers of larvae interact in close proximity [36, 37]. Beyond this, there are several potential applications in both biology and engineering. For instance, our findings could aid in the development of quantitative assays for studying larval morphological changes in response to chemicals [38], as well as ecological assays to assess microplastics accumulation in marine zooplankton [39, 40]. In engineering applications, these insights from ciliary flows could contribute to the design of microfluidic devices like lab-on-a-chip systems [41], artificial water purification devices [42, 43], and

morphologically optimized micro-robots for targeted drug delivery [44], environmental monitoring [45], and beyond.

## Methods

### Laboratory cultures of marine larvae and algae

Adult sea stars (bat stars, *Patiria miniata*) were collected and shipped to Miami from the California coast (Marinus Scientific, CA), and males and females were kept separately in two 20-gallon glass aquarium tanks. The aquariums were assembled from commercially available standard components (Petco). Each aquarium tank was filled with seawater (Imagitarium pacific ocean water, Petco) and maintained at a temperature of 16.6°C using an external chiller unit. The tank seawater was continuously circulated using a pump and filtered, and regular water changes (90% replacement) were carried out monthly. The sea stars were fed cut pieces of supermarket-purchased shrimp once a month.

The larvae were fed with marine algae, both red algae (*Rhodomonas lens*, *Rhodomonas salina*) and green algae (*Dunaliella tertiolecta*), which were obtained from the National Center for Marine Algae and Microbiota (NCMA, Bigelow, ME). The algae were cultured in erlenmeyer flasks containing filtered seawater and nutrients (Micro Algae Grow, Florida Aqua Farms) in 1:100 dilution and kept in an incubator maintained at a temperature of 14°C, under 12 hour dark/light cycles using LED lighting. The algae flasks were shaken at least once daily to prevent settling at the bottom, and the algae cultures were split weekly into 1:4 volumes of fresh seawater and nutrients.

### Spawning of marine larvae

In-vitro fertilization of the sea star (*Patiria miniata*) gametes were carried out in glass dishes. The eggs collected from the female sea stars were kept in 100  $\mu$ M 1-methyladenine (1-MA) to mature eggs for about 30-60 minutes. Then freshly collected sperm from the males were added (1:1000 dilution) and gently mixed in the seawater using a plastic pipette. After successful fertilization, the glass dishes containing growing embryos were placed in incubators maintained at a temperature of 16.6° C. The red and green marine algae *R. lens*, *R. salina*, *D. tertiolecta*) were provided as a food source for growing larvae, and regular water changes were carried out weekly. The sea urchin larvae (*Lytechinus variegatus*) were obtained from the animal culture facility at The National Resource for Aplysia on the campus of University of Miami's Rosenstiel School of Marine, Atmospheric, and Earth Science.

### Larval mounting and live imaging experiments

A larva was confined or squeezed gently between a bottom glass slide and a top cover slip with different heights (z-direction) using a spacer tape, and fluid flow-fields were quantified in a quasi-2D x-y plane. Glass slides were first prepared by attaching a pair of long rectangular strips of double-sided tape of different thicknesses 50/100/150  $\mu$ m (Nitto Inc.) on the slide edges to serve as spacers for a required boundary height (H).

Using this method, the boundary height (H) was varied systematically up to 900  $\mu\text{m}$ , with minimum increments of 50  $\mu\text{m}$ .

A small droplet ( $\sim 50\mu\text{L}$ ) of seawater containing the larva of interest was transferred using a micropipette from the culture dish into the center of the prepared glass slide with the spacers at the edges. A smaller droplet ( $\sim 10\mu\text{L}$ ) containing  $1\mu\text{m}$ -sized tracer polystyrene microspheres (Polysciences Inc, with 1:100 dilution in seawater) was added to the droplet with the larva and gently mixed.

A cover slip was introduced slowly onto the glass slide containing the larva and microspheres, and attached on the spacer tapes at the edges. Next, live-imaging experiments were carried out by mounting this glass slide on an upright microscope (Zeiss Axio Imager M2). The microsphere movements were imaged using darkfield time-lapse imaging using a 10X objective to capture a  $1.5\text{ mm} \times 1.5\text{ mm}$  field of view. The time-lapse images were acquired at 10 fps for a duration of 30 s using a high-speed camera (Hamamatsu ORCA-Fusion Gen-III sCMOS) attached to the Zeiss microscope.

## Experimental data post-processing and analysis

The larval flow-fields were qualitatively visualized using the Flowtrace technique [32]. The flowtrace analysis was run using the image-J plugin for 30 s durations over a time-averaging window of 3 s. Flowtrace visualizations were carried out on all the experimental datasets, and these videos were used to count the number of vortices (number of closed circular pathlines) for each case of confinement. The number of vortices was noted for the entire 30 s time sequence of a single dataset, and then an average was taken over at least  $N = 3$  samples to represent the average number of vortices for each case of confinement and larva. The total number of datasets analyzed for Early-stage sea stars, Late-stage sea stars and Sea urchin larvae are  $N = 55, 44,$  and 26 respectively (Table 1, Supplementary Information).

The Particle Image Velocimetry (PIV) technique was adopted for quantification of the experimental larval flows. The time-lapse images were post-processed using PIVlab in MATLAB [33]. A mask was drawn in PIVlab over the larva to avoid any flow quantification noisy artifacts inside the larval body. The time-lapse images were first pre-processed to remove background noise using high-pass filters. Then the images were subjected to the PIV analysis where the time-varying velocity vector fields are computed. These velocity fields were further processed to smoothen and interpolate the vector fields as necessary. Next, the flow parameters such as vorticity or velocity magnitude were plotted along with the velocity vector fields. The averaged mean of parameters such as vorticity or velocity magnitude were calculated over a time window of 3 s in order to obtain smooth fluid flow visualizations and quantification. The distance from the center of vortices to the larval body surface was measured in  $N = 3$  larval datasets and averaged to obtain the average distance measurements.

## Theoretical model for confinement-induced flows

In order to theoretically model fluid flows generated by the ciliated marine larvae under squeeze-confinement, we used an approach utilizing superposition of Stokeslets [6, 7]. In the experiments, the ciliated larvae were confined between two plates and

the flows were measured at the midplane, i.e.  $z = H/2$ . Recently, flow fields generated by a *Chlamydomonas* confined between two parallel plates was studied using both experiments and theory [7]. Inspired by this work, we extended the theoretical model and applied to our experiments in ciliated marine larvae. The theoretical model starts with the incompressible 3D Stokes equation (as in Ref [7]),

$$\nabla p(r) + \eta \nabla^2 v(r) = 0, \nabla \cdot v(r) = 0. \quad (1)$$

where  $p$  and  $v$  are the fluid pressure and velocity fields respectively. Next, based on the quasi-2D Brinkman approximation, the equations are rewritten as

$$\nabla_{xy} p(r) + \eta \left( \nabla_{xy}^2 - \frac{\pi^2}{H^2} \right) v(r) + F \delta(r) = 0, \nabla_{xy} \cdot v(r) = 0. \quad (2)$$

where  $F$  is the point source of force generation in the  $z = H/2$  plane. The solution to the above equation (using Fourier analysis) is obtained as:

$$\begin{bmatrix} v_x \\ v_y \end{bmatrix} (r, \phi) = \frac{F}{2\pi^2\eta} \int_{-\pi/2+\phi}^{\pi/2+\phi} d\theta \int_0^\infty dk \begin{bmatrix} \sin^2 \theta \\ \sin \theta \cos \theta \end{bmatrix} \frac{k \cos [kr \cos(\theta - \phi)]}{(k^2 + \frac{\pi^2}{H^2})} \quad (3)$$

The velocity fields are numerically solved over a  $30 \times 30$  x-y grid in MATLAB to obtain the theoretical flow-fields. In Ref [7], the *Chlamydomonas* has two flagella that beat to generate vortices, however, here the marine larvae generate fluid vortices using a large number of cilia located on their ciliary bands. Although the methods of inducing fluid flow are different in the two studies, the consequence, i.e. vortex generation, is the same in both cases. Here, the focus is on modeling the overall flow-fields induced by confinement rather than the local mechanism of vorticity generation.

A unit Stokeslet is used to model the flow field corresponding to a single vortex. To account for the multiple vortices that are developed in the experiments, we superpose multiple Stokeslets (corresponding to each vortex) on the same physical locations on the larval body (determined from experiments) and obtain the resultant theoretical velocity field. Further details on the theoretical model, including the procedure for introduction of multiple Stokeslets for each type of larvae, and their corresponding flow fields are provided in the supplementary material.

**Supplementary information.** Supplementary information for this manuscript include the following items:

Videos 1 and 2.

PDF file with supporting text, Figures S1-S4, Tables SX-SX, and Video Legends.

**Acknowledgements.** We thank present and past Prakash lab members for their helpful suggestions and support. We thank Zak Swartz (Marine Biological laboratory) and Athula Wikramanayake (University of Miami) for help with sea star culturing. We thank Phillip Gilette (University of Miami Rosenstiel School) for providing the sea urchin larvae. We thank Nitto Inc. (Atlanta, GA) for generously providing the spacer

tapes used in our experiments. We thank Maciej Lisicki (University of Warsaw) and Lyndon Koens (University of Hull) for their invaluable suggestions on the theoretical modeling. V.N.P. thanks Manu Prakash (Stanford University) and William Gilpin (University of Texas at Austin) for many insightful discussions over the years.

C.D.G. acknowledges funding support from the Florida-Georgia Louis Stokes Alliance for Minority Participation (FGLSAMP) undergraduate research program funded by the National Science Foundation (NSF) (grant #0217675). V.N.P. acknowledges Start-up funding support and a Provost's Research Award from the University of Miami.

### **Author Contributions.**

Conceptualization: B.D.S., S.C., V.N.P.  
Methodology - experiments: B.D.S., C.D.G., N.R.C.  
Methodology - theory: S.C.  
Data Analysis: B.D.S., S.C., M.R.  
Writing – original draft: B.D.S., S.C., V.N.P.  
Writing – review, editing: B.D.S., S.C., M.R., V.N.P.  
Supervision: V.N.P.  
Project Administration: V.N.P.  
Funding Acquisition: V.N.P.

**Competing Interests.** The authors do not have any competing interests.

**Materials & Correspondence.** Author to whom correspondence and materials requests should be addressed: V.N.P. E-mail: vprakash@miami.edu

**Data availability.** The data that support the results from this study are available from the corresponding author on request.

**Code availability.** The computer codes that support the results from this study are available from the corresponding author on request.

## **References**

- [1] Sardet, C.: Plankton: Wonders of the Drifting World. University of Chicago Press, ??? (2020)
- [2] Lauga, E., Powers, T.R.: The hydrodynamics of swimming microorganisms. Reports on progress in physics **72**(9), 096601 (2009)
- [3] Gilpin, W., Bull, M.S., Prakash, M.: The multiscale physics of cilia and flagella. Nature Reviews Physics **2**(2), 74–88 (2020)

- [4] Emlet, R.B.: Functional constraints on the evolution of larval forms of marine invertebrates: experimental and comparative evidence. *American Zoologist* **31**(4), 707–725 (1991)
- [5] Gilpin, W., Prakash, V.N., Prakash, M.: Vortex arrays and ciliary tangles underlie the feeding–swimming trade-off in starfish larvae. *Nature Physics* **13**(4), 380–386 (2017)
- [6] Liron, N., Mochon, S.: Stokes flow for a stokeslet between two parallel flat plates. *Journal of Engineering Mathematics* **10**(4), 287–303 (1976)
- [7] Mondal, D., Prabhune, A.G., Ramaswamy, S., Sharma, P.: Strong confinement of active microalgae leads to inversion of vortex flow and enhanced mixing. *Elife* **10**, 67663 (2021)
- [8] Denny, M.W.: *Air and Water: the Biology and Physics of Life’s Media*. Princeton University Press, ??? (1993)
- [9] Vogel, S.: *Life in Moving Fluids: the Physical Biology of Flow*—revised and Expanded Second Edition. Princeton university press, ??? (2020)
- [10] Dabiri, J.O.: Landmarks and frontiers in biological fluid dynamics. *Physical Review Fluids* **4**(11), 110501 (2019)
- [11] Wan, K.Y.: Life through the fluid dynamics lens. *Nature Physics* **19**(12), 1744–1745 (2023)
- [12] Byron, M.L., Murphy, D.W., Katija, K., Hoover, A.P., Daniels, J., Garayev, K., Takagi, D., Kanso, E., Gemmel, B.J., Ruszczyk, M., *et al.*: Metachronal motion across scales: current challenges and future directions. *Integrative and comparative biology* **61**(5), 1674–1688 (2021)
- [13] Gilpin, W., Prakash, V.N., Prakash, M.: Dynamic vortex arrays created by starfish larvae. *Physical Review Fluids* **2**(9), 090501 (2017)
- [14] Ishikawa, T.: Fluid dynamics of squirmers and ciliated microorganisms. *Annual Review of Fluid Mechanics* **56**(1), 119–145 (2024)
- [15] Pepper, R.E., Roper, M., Ryu, S., Matsudaira, P., Stone, H.A.: Nearby boundaries create eddies near microscopic filter feeders. *Journal of the Royal Society Interface* **7**(46), 851–862 (2010)
- [16] Pepper, R.E., Roper, M., Ryu, S., Matsumoto, N., Nagai, M., Stone, H.A.: A new angle on microscopic suspension feeders near boundaries. *Biophysical journal* **105**(8), 1796–1804 (2013)
- [17] Shekhar, S., Guo, H., Colin, S.P., Marshall, W., Kanso, E., Costello, J.H.: Cooperative hydrodynamics accompany multicellular-like colonial organization in the

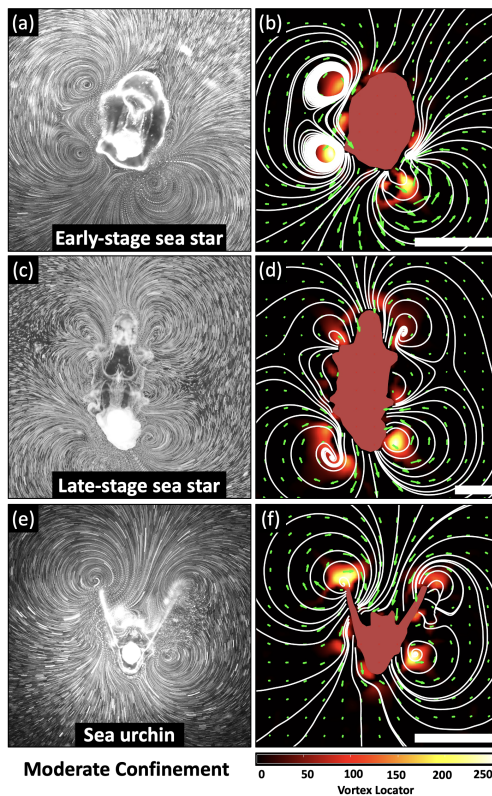


unicellular ciliate stentor. *bioRxiv* (2023)

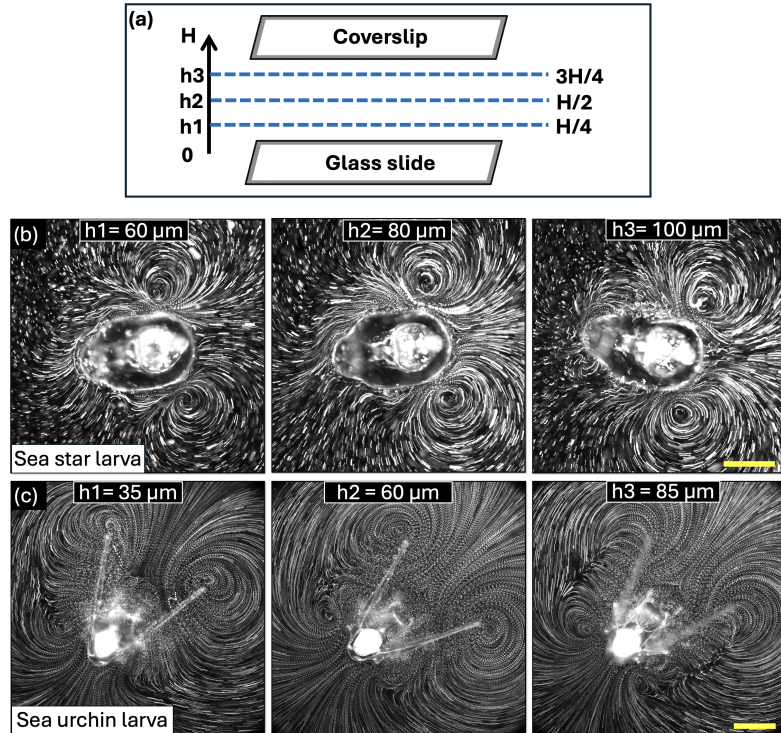
- [18] Shapiro, O.H., Fernandez, V.I., Garren, M., Guasto, J.S., Debaillon-Vesque, F.P., Kramarsky-Winter, E., Vardi, A., Stocker, R.: Vortical ciliary flows actively enhance mass transport in reef corals. *Proceedings of the National Academy of Sciences* **111**(37), 13391–13396 (2014)
- [19] Kiel, P.M., Prakash, V.N.: Coral physiology: Going with the ciliary flow. *Current Biology* **32**(19), 998–1000 (2022)
- [20] Ling, F., Essock-Burns, T., McFall-Ngai, M., Katija, K., Nawroth, J.C., Kanso, E.: Flow physics guides morphology of ciliated organs. *Nature Physics* **20**(10), 1679–1686 (2024)
- [21] Emlet, R.B.: Flow fields around ciliated larvae: Effects of natural and artificial tethers. *Marine ecology progress series. Oldendorf* **63**(2), 211–225 (1990)
- [22] Catton, K.B., Webster, D.R., Brown, J., Yen, J.: Quantitative analysis of tethered and free-swimming copepodid flow fields. *Journal of Experimental Biology* **210**(2), 299–310 (2007)
- [23] Mathijssen, A.J., Doostmohammadi, A., Yeomans, J.M., Shendruk, T.N.: Hydrodynamics of micro-swimmers in films. *Journal of Fluid Mechanics* **806**, 35–70 (2016)
- [24] Dassow, G., Emler, R., Grünbaum, D.: Boundary effects on currents around ciliated larvae. *Nature Physics* **13**(6), 520–521 (2017)
- [25] Gilpin, W., Prakash, V.N., Prakash, M.: Reply to ‘boundary effects on currents around ciliated larvae’. *Nature Physics* **13**(6), 521–522 (2017)
- [26] Jeanneret, R., Pushkin, D.O., Polin, M.: Confinement enhances the diversity of microbial flow fields. *Physical Review Letters* **123**(24), 248102 (2019)
- [27] Bentley, S.A., Laeverenz-Schlogelhofer, H., Anagnostidis, V., Cammann, J., Mazza, M.G., Gielen, F., Wan, K.Y.: Phenotyping single-cell motility in microfluidic confinement. *Elife* **11**, 76519 (2022)
- [28] Bondoc-Naumovitz, K.G., Laeverenz-Schlogelhofer, H., Poon, R.N., Boggon, A.K., Bentley, S.A., Cortese, D., Wan, K.Y.: Methods and measures for investigating microscale motility. *Integrative and Comparative Biology* **63**(6), 1485–1508 (2023)
- [29] Selvan, S.A., Duck, P.W., Pihler-Puzović, D., Brumley, D.R.: Point torque representations of ciliary flows. *Physical Review Fluids* **8**(12), 123103 (2023)
- [30] N. Radhakrishnan, B., Purushothaman, A., Dey, R., Thampi, S.P.: Confinement induced three-dimensional trajectories of microswimmers in rectangular channels.

- [31] Krishnamurthy, D., Li, H., Rey, F., Cambournac, P., Larson, A.G., Li, E., Prakash, M.: Scale-free vertical tracking microscopy. *Nature Methods* **17**(10), 1040–1051 (2020)
- [32] Gilpin, W., Prakash, V.N., Prakash, M.: Flowtrace: simple visualization of coherent structures in biological fluid flows. *Journal of Experimental Biology* **220**(19), 3411–3418 (2017)
- [33] Stamhuis, E., Thielicke, W.: Pivlab—towards user-friendly, affordable and accurate digital particle image velocimetry in matlab. *Journal of open research software* **2**(1), 30 (2014)
- [34] Stamhuis, E.J.: Basics and principles of particle image velocimetry (piv) for mapping biogenic and biologically relevant flows. *Aquatic Ecology* **40**(4), 463–479 (2006)
- [35] Mazia, D., Schatten, G., Sale, W.: Adhesion of cells to surfaces coated with polylysine. applications to electron microscopy. *The Journal of cell biology* **66**(1), 198–200 (1975)
- [36] Tan, T.H., Mietke, A., Li, J., Chen, Y., Higinbotham, H., Foster, P.J., Gokhale, S., Dunkel, J., Fakhri, N.: Odd dynamics of living chiral crystals. *Nature* **607**(7918), 287–293 (2022)
- [37] Bárdfalvy, D., Škultéty, V., Nardini, C., Morozov, A., Stenhammar, J.: Collective motion in a sheet of microswimmers. *Communications Physics* **7**(1), 93 (2024)
- [38] Lion, A.T., Bodine, S.M., McCutcheon, K.R., Ghogale, M., Chandragiri, S., Abayawardena, D., Shrestha, B.D., Descoteaux, A.E., Alvarez, K., Balkman, J.A., et al.: Pfas compounds pfoa and gen x are teratogenic to sea urchin embryos. *bioRxiv*, 2024–11 (2024)
- [39] Law, K.L., Thompson, R.C.: Microplastics in the seas. *Science* **345**(6193), 144–145 (2014)
- [40] Botterell, Z.L., Beaumont, N., Dorrington, T., Steinke, M., Thompson, R.C., Lindeque, P.K.: Bioavailability and effects of microplastics on marine zooplankton: A review. *Environmental Pollution* **245**, 98–110 (2019)
- [41] Cui, Z., Wang, Y., Zhang, S., Wang, T., Toonder, J.M.: Miniaturized metachronal magnetic artificial cilia. *Proceedings of the National Academy of Sciences* **120**(35), 2304519120 (2023)
- [42] Rubenstein, D.I., Koehl, M.A.: The mechanisms of filter feeding: some theoretical considerations. *The American Naturalist* **111**(981), 981–994 (1977)

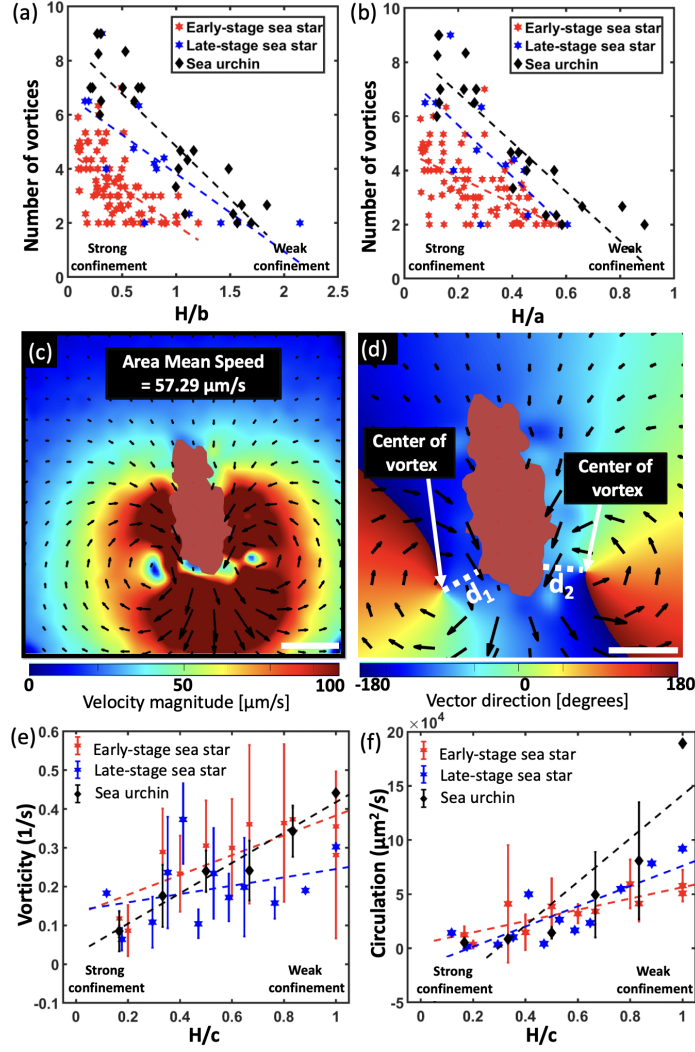
- [43] Urso, M., Ussia, M., Pumera, M.: Smart micro-and nanorobots for water purification. *Nature Reviews Bioengineering* **1**(4), 236–251 (2023)
- [44] Dillinger, C., Nama, N., Ahmed, D.: Ultrasound-activated ciliary bands for microrobotic systems inspired by starfish. *Nature communications* **12**(1), 6455 (2021)
- [45] Soto, F., Karshalev, E., Zhang, F., Avila, B., Nourhani, A., Wang, J.: Smart materials for microrobots. *Chemical Reviews* **122**(5), 5365–5403 (2021)



**Extended Data Fig. 1: Fluid flow vortices around ciliated marine larvae under moderate squeeze confinement in experiments.** Left panels show Flowtrace visualization of fluid flow around the larvae, and right panels show the PIV-derived streamlines (white) along with the velocity vector field (green arrows) that are superimposed on the vortex locator (color contour). (a) An early-stage sea star larva creates 3 vortices under moderate confinement ( $H/c = 0.8$ ). (b) A late-stage sea star larva creates 4 vortices under moderate confinement ( $H/c = 0.4$ ). (c) A sea urchin larva creates 3 vortices under moderate confinement ( $H/c = 0.8$ ). The length scale bars (white) correspond to 0.4 mm.

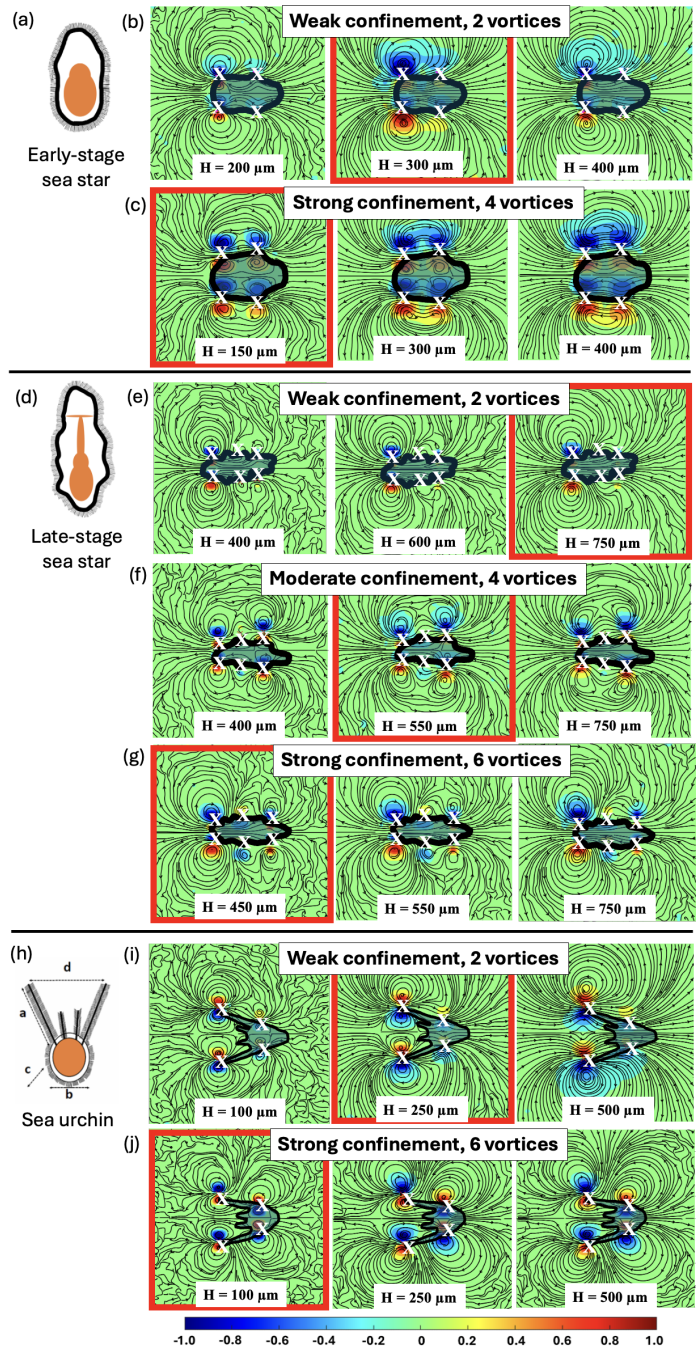


**Extended Data Fig. 2: Fluid flow-fields around squeeze-confined marine larvae at different z-planes.** (a) Schematic representation of the different z-planes of imaging between a glass slide and a cover slip on a microscope. (b) Flowtrace visualization around an Early-stage sea star larva at three z-planes (chamber height,  $H = 150 \mu\text{m}$ ). (c) Flowtrace visualization around a Sea urchin larva at three z-planes (chamber height,  $H = 100 \mu\text{m}$ ). The length scale bars in (b,c) (yellow) correspond to 0.2 mm.



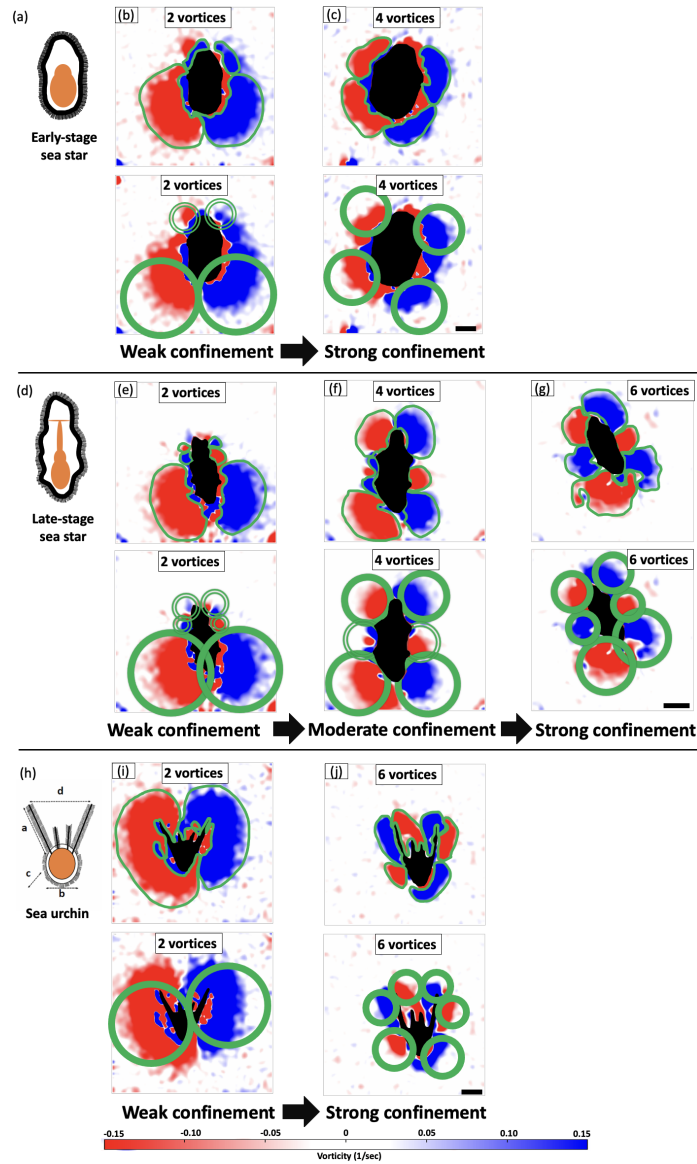
**Extended Data Fig. 3: Quantification of flow parameters in experiments.** (a,b) Scatter plots of the total number of vortices generated by Early-stage sea star, Late-stage sea star, and Sea urchin larvae as a function of normalized heights  $H/b$  (a) and  $H/a$  (b). Here, 'b' and 'a' are the length scales of larval height and width (schematic cartoons in Fig. 1). The dotted lines are linear fits to the data for each type of larva. (c) The velocity magnitude heatmap around a Late-stage sea star larva obtained through PIVlab [33] is shown (color bar below). (d) The vector direction heatmap around a Late-stage sea star larva is shown.  $d_1$  and  $d_2$  represent the closest distances from the centers of vortices to the larval body. (e,f) The average vorticity and average circulation is plotted as a function of the normalized squeeze parameter ( $H/c$ ) for the three types of larvae. The data points indicate mean values and errorbars indicate standard deviations, and dotted lines indicate linear fits to the mean values for each type of larva. The length scale bars in (c,d) (white) correspond to 0.5mm.





**Extended Data Fig. 4: Theoretical flow-fields around marine larvae under different confinements.** In each panel, the black lines with arrows are streamlines and the heatmap represents vorticity contours. Theoretical panels closely matching experimental data one-on-one at specific heights are highlighted in red boxes. (a) Early-stage sea star larva: Theoretical flow fields under weak and strong confinement. (b) Late-stage sea star larva: Theoretical flow fields under weak, moderate, and strong confinement. (c) Sea urchin larva: Theoretical flow fields under weak and strong confinement. The vorticity is normalized for each case (Supplementary Material) and their magnitudes are indicated in the color bar shown below.





**Extended Data Fig. 5: Quantifying vortex size around marine larvae under different confinements in experiments.** All panels represent the vorticity heatmap (red/blue colorbar below) with 'patches' of vorticity generated by the larvae. Top row: vorticity patches are marked with green boundaries, whose areas are quantified manually. Bottom row: vorticity patches are marked with circles representing the equivalent diameter based on the calculated area from top row. The solid green circles indicate the dominant vortices that can be readily visualized (Figures 1,2), and the 'dashed/thin' circles represent equivalent vortices that are neither dominant nor seen visually in the experiments. (a) Early-stage sea star larva under weak (b) and strong (c) confinements. (d) Late-stage sea star larva under weak (e), moderate (f), and strong (g) confinements. (h) Sea urchin larva under weak (i) and strong (j) confinements.